thermo

MDPI

Article

Thermodynamic Performance and Response-Surface Optimization of an Integrated HT-PEMFC–Organic Rankine Cycle System for Low-Grade Waste-Heat Recovery

Faisal Albatati [1], Abdelkarim Hegab [1,*], Asad A. Zaidi [2,*], Aisha Jilani [3] and Faisal J. Alzahrani [1]

[1] Mechanical Engineering Department, Faculty of Engineering, King Abdulaziz University, Rabigh 25732, Saudi Arabia; alalbatati@kau.edu.sa (F.A.); fjsalzahrani@kau.edu.sa (F.J.A.)
[2] Department of Mechanical Engineering, Faculty of Engineering, Islamic University of Madinah, Madinah 42351, Saudi Arabia
[3] Faculty of Chemical and Process Engineering, NED University of Engineering and Technology, Karachi 75270, Pakistan; aishajilani@neduet.edu.pk
* Correspondence: amhegab@kau.edu.sa (A.H.); sali@iu.edu.sa (A.A.Z.)

Abstract

High-temperature proton-exchange membrane fuel cells (HT-PEMFCs) generate useful thermal energy that can be recovered for additional power production. This study investigates an integrated HT-PEMFC–organic Rankine cycle (ORC) system by combining response surface methodology (RSM) with thermodynamic energy analysis. A 17-run response-surface design was used to quantify the effects of pressure, temperature, and current density on polarization voltage. Power density was derived directly from the RSM-predicted voltage using P_d = iE to preserve physical consistency. The electrochemical model was benchmarked against published phosphoric-acid-doped polybenzimidazole HT-PEMFC polarization data under comparable conditions. The constrained optimization identified an operating condition of 400 kPa, 443 K, and approximately 1.198 A cm^{-2}, giving a predicted voltage of 0.5395 V and a power density of approximately 0.6462 W cm^{-2}. This represents a 12.9% increase in power density relative to the adopted reference condition. Separately, the reference thermodynamic case produced 13.08 kW of gross HT-PEMFC stack electrical power and 15.45 kW of thermal output assumed available to the ORC. The available legacy R409A reference case was evaluated at an evaporator pressure of 2 MPa, yielding approximately 1.24 kW of ORC net power and a net thermal efficiency of about 8.02%. The resulting combined modeled electrical output was approximately 14.32 kW before unmodeled balance-of-plant auxiliary power consumption, with the ORC contribution corresponding to about 9.5% of the gross HT-PEMFC stack output. The results demonstrate the complementary potential of physically consistent HT-PEMFC operating-condition optimization and waste-heat recovery, while the ORC results remain specific to the retained R409A reference dataset.

Keywords: high-temperature proton-exchange membrane fuel cell; organic Rankine cycle; waste-heat recovery; response surface methodology; zeotropic working fluid; thermodynamic analysis; power density

Check for updates

Academic Editors: Muhammad Faizan Tahir, Luca Cimmino and Francesco Calise

Received: 22 August 2026
Revised: 5 September 2026
Accepted: 8 September 2026
Published: 10 September 2026

Copyright: © 2026 by the authors. Licensee MDPI, Basel, Switzerland. This article is an open access article distributed under the terms and conditions of the Creative Commons Attribution (CC BY) license.

1. Introduction

The transition toward efficient and low-carbon energy-conversion technologies has intensified interest in hydrogen-fueled electrochemical power systems. Among the available fuel-cell technologies, proton-exchange membrane fuel cells (PEMFCs) are particularly

attractive because of their high power density, modular construction, rapid response, and ability to convert the chemical energy of hydrogen directly into electricity without an intermediate combustion process [1,2]. Nevertheless, a considerable fraction of the fuel-energy input is ultimately released as thermal energy rather than electrical work. Effective thermal management is therefore important not only for maintaining stable fuel-cell operation but also for improving overall energy utilization through recovery of otherwise rejected heat [3–5].

High-temperature proton-exchange membrane fuel cells (HT-PEMFCs) provide particular advantages for thermal integration. In contrast with conventional low-temperature PEMFCs, HT-PEMFCs typically operate at elevated temperatures and commonly employ phosphoric-acid-doped polybenzimidazole-based proton-conducting membranes [6]. Their elevated operating temperature simplifies water management, improves tolerance to fuel impurities, facilitates heat rejection, and provides waste heat at a more useful temperature level for downstream thermal processes [3,7]. Recent work has addressed membrane development, thermal management, and durability in HT-PEMFCs [3,4,7–9]. In parallel, fuel-cell waste-heat recovery has received increasing attention as a means of improving overall energy utilization [10,11].

Among the available technologies for low- and medium-temperature heat-to-power conversion, the organic Rankine cycle (ORC) is particularly suitable because organic working fluids can undergo phase change at substantially lower temperatures than water [12]. ORCs have therefore been widely investigated for industrial waste heat, geothermal heat, engine exhaust, solar thermal energy, and other low-grade thermal sources [13,14]. The thermodynamic performance of an ORC is strongly dependent on the properties of the working fluid and on the temperature matching between the heat source and the evaporation process. Zeotropic mixtures are of particular interest because their non-isothermal phase-change behavior can improve temperature matching in heat exchangers and potentially reduce heat-transfer irreversibility compared with an inadequately matched pure fluid [13,15]. Consequently, working fluid selection, evaporator pressure, heat-source temperature, and component efficiencies remain central considerations in designing ORCs for relatively low-temperature waste-heat recovery [16].

The present work addresses the thermodynamic and electrochemical integration of an HT-PEMFC with an ORC for waste-heat recovery, with particular attention to the operating conditions of the fuel cell itself. The subject is therefore not limited to ORC working-fluid selection or bottoming-cycle optimization. Instead, the study examines how HT-PEMFC pressure, temperature, and current density affect polarization voltage and power density and how a suitable electrochemical operating region can be identified while preserving the temperature potential required for downstream heat recovery. This coupling between electrochemical operation and thermal recovery forms the central subject of the present investigation.

Several previous studies have demonstrated the benefits of PEMFC–ORC integration [17,18]. Wang et al. [18] developed a PEMFC waste-heat recovery system using a zeotropic ORC and showed that working-fluid composition and operating conditions strongly affect system performance. Their study demonstrated that zeotropic mixtures can improve net power and system efficiency and established the importance of working-fluid selection for fuel-cell waste-heat recovery. However, the analysis mainly focused on thermodynamic performance, working-fluid selection, and conventional parametric effects. It did not statistically quantify the individual, interaction, and nonlinear effects of fuel-cell operating variables on electrochemical responses such as polarization voltage and power density. Lu et al. [19] extended PEMFC–ORC analysis by considering steady-state, dynamic, and economic performance and by recovering heat from several fuel-cell-system

streams. This provided a broader system-level assessment and demonstrated the practical value of multi-stream heat recovery. Nevertheless, the main emphasis remained on overall CHP-system performance and dynamic behavior rather than detailed statistical optimization of the electrochemical operating conditions of the fuel-cell stack.

More recent studies have incorporated advanced optimization and specifically considered HT-PEMFC systems. Zhou et al. [20] evaluated a PEMFC–ORC cogeneration system using energy, exergy, and economic indicators together with multi-objective optimization. This provided a useful system-level balance between electrical and economic performance, but the study did not focus on resolving the combined effects of HT-PEMFC pressure, temperature, and current density. Taweekayujan et al. [21] integrated methanol reforming, an HT-PEMFC, and an ORC and carried out detailed energy, exergy, and exergoeconomic analyses. Their broader fuel-processing configuration and economic objectives differ from the present focus on direct HT-PEMFC operating-condition optimization and recovery of available stack heat. Xu et al. [22] proposed an HT-PEMFC coupled with a recuperative-regenerative ORC and performed energy, exergy, economic, and two-objective optimization. Their work demonstrated the potential of an advanced ORC configuration, but the optimization was directed mainly toward overall system design rather than a response-surface representation of the HT-PEMFC electrochemical operating variables. Experimental ORC studies have also examined operation under periodically varying waste-heat conditions, highlighting the importance of heat-source characteristics for practical waste-heat recovery [23].

Together, these studies demonstrate the thermodynamic value of PEMFC–ORC and HT-PEMFC–ORC integration, but most previous work has emphasized cycle configuration, working-fluid selection, overall system thermodynamics, economic assessment, or multi-objective system optimization. Comparatively less attention has been given to quantitatively characterizing the simultaneous linear, interaction, and nonlinear effects of pressure, temperature, and current density on HT-PEMFC polarization voltage while also imposing a thermal constraint associated with downstream waste-heat recovery. The present study addresses this gap by using response surface methodology to develop a fitted surrogate model for polarization voltage. Power density is then derived directly from the predicted voltage through $P_d = iE$, thereby preserving physical consistency during constrained optimization.

Accordingly, the present study evaluates a thermally integrated HT-PEMFC–ORC system in which stack waste heat is used for additional power generation. Pressure, temperature, and current density are treated as the HT-PEMFC operating variables, while polarization voltage is modeled through a Box–Behnken-based response-surface design. Power density is calculated directly from the predicted voltage using $P_d = iE$, and the resulting physically consistent function is used for constrained optimization. Separately, the available R409A reference thermodynamic case is evaluated using energy analysis to quantify the ORC power obtained from the stack thermal output assumed available for recovery.

The principal contribution of this work is the combined assessment of physically consistent HT-PEMFC operating-condition optimization and reference-case thermodynamic waste-heat recovery. Specifically, the study (i) quantifies the linear, interaction, and nonlinear effects of pressure, temperature, and current density on polarization voltage; (ii) derives power density directly from the fitted voltage response and identifies a constrained operating condition; (iii) evaluates the retained R409A ORC reference case using energy analysis; and (iv) quantifies the ORC net power contribution relative to the gross HT-PEMFC stack output. The RSM optimization and ORC thermodynamic analysis are

treated as complementary parts of the overall system assessment, while the ORC results remain limited to the retained reference dataset.

2. System Description and Mathematical Modeling

2.1. Integrated HT-PEMFC–ORC Configuration

The proposed system integrates an HT-PEMFC with an ORC to recover a portion of the thermal energy rejected during electrochemical power generation. The HT-PEMFC constitutes the primary energy-conversion unit, converting the chemical energy of supplied hydrogen directly into electrical power, while the ORC operates as a bottoming cycle driven by the recoverable thermal output of the fuel-cell stack. Such thermal integration enables simultaneous utilization of the electrical and thermal fractions of the fuel-energy input and provides additional power generation without requiring supplementary fuel consumption [19,21].

The configuration of the integrated system is illustrated in Figure 1. Hydrogen and oxygen are supplied to the anode and cathode sides of the HT-PEMFC stack, respectively. Electrochemical oxidation of hydrogen and reduction of oxygen generate direct-current electrical power, whereas the difference between the thermochemical energy supplied to the stack and the useful electrical output appears predominantly as heat. In the proposed configuration, part of this rejected thermal energy is transferred to the ORC working fluid through an evaporator/heat exchanger instead of being discharged directly to the surroundings.

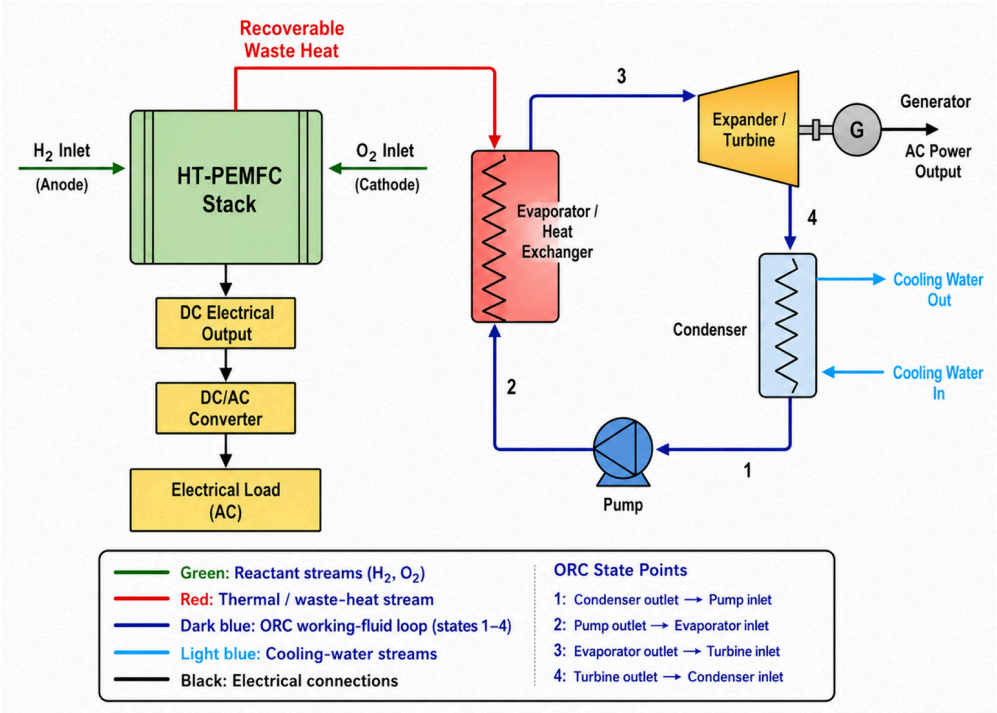


Figure 1. Schematic configuration of the integrated HT-PEMFC–ORC system for waste-heat recovery and additional power generation. The DC/AC converter and generator are shown schematically; their conversion losses are not included in the modeled electrical output.

The ORC consists principally of a pump, evaporator/heat exchanger, expander coupled to an electrical generator, and condenser. The thermodynamic states of the ORC working fluid are denoted by states 1–4 in Figure 1. At state 1, the condensed working fluid enters the pump as a saturated liquid. The pump increases the fluid pressure to the prescribed evaporator pressure, producing the compressed-liquid condition at state 2. Because

the actual pumping process is non-isentropic, a finite amount of electrical or mechanical work is required to overcome the pressure difference across the cycle.

From state 2, the high-pressure working fluid enters the evaporator/heat exchanger, where thermal energy rejected by the HT-PEMFC is transferred to the ORC. Heat transfer increases the enthalpy of the working fluid and produces a high-pressure vapor at state 3. The evaporator therefore provides the direct thermodynamic coupling between the HT-PEMFC and the ORC.

The high-pressure vapor at state 3 subsequently expands through the expander to state 4. The decrease in working-fluid enthalpy during expansion is converted into shaft work, which is subsequently converted into electrical power by the coupled generator. The actual expansion process is non-isentropic because of internal irreversibilities; accordingly, the actual expander work is lower than that corresponding to an ideal isentropic expansion between the same pressure limits. The working fluid leaving the expander is then directed to the condenser, where heat is rejected to the cooling medium until the fluid returns to the saturated-liquid condition at state 1, thereby completing the thermodynamic cycle.

The thermodynamic coupling between the two subsystems is governed by the quantity and temperature level of heat rejected by the fuel-cell stack. These quantities are themselves affected by HT-PEMFC operating parameters, particularly temperature, pressure, and current density. Consequently, changes in the electrochemical operating point influence not only the electrical power delivered by the HT-PEMFC but also the thermal energy available to drive the ORC. This interaction provides the basis for combining fuel-cell operating-condition optimization with subsequent thermodynamic analysis of the heat-recovery cycle rather than treating the two subsystems as completely independent units.

For the ORC subsystem, R409A is retained as the working fluid because the available reference thermodynamic dataset was developed using this mixture. Its use and relevant phase-change characteristics are described in Section 2.4. The steady-state energy relations for the pump, evaporator, expander, and condenser, together with the ORC net-power and thermal-efficiency formulations, are presented in Section 2.5.

2.2. HT-PEMFC Electrochemical Model

The electrochemical subsystem considered in this study is an HT-PEMFC based on a phosphoric-acid-doped polybenzimidazole (PBI) membrane. PBI-based membranes are suitable for elevated-temperature PEMFC operation because proton conduction can be maintained through phosphoric acid without the intensive membrane humidification required by conventional low-temperature PEMFCs [3]. The elevated operating temperature also facilitates heat rejection and provides a thermally useful heat source for coupling with the ORC considered in this work. Recent investigations have demonstrated that HT-PEMFC performance remains strongly dependent on operating temperature, reactant conditions, and current density, which influence electrochemical kinetics, transport resistance, and polarization behavior [24,25].

The electrochemical formulation follows the standard Nernst, Tafel, ohmic, and concentration-polarization framework commonly used for PEMFC analysis [26]. The membrane properties were adopted from Jayakody et al. [27], who reported a phosphoric-acid-to-PBI molar ratio of 12.2 and a proton conductivity of 0.048 S cm^{-1} at 160 °C for conventionally imbibed PBI. The same study estimated an upper bound of approximately 1×10^{-7} cm^2 s^{-1} for proton self-diffusion in this membrane.

At the anode, hydrogen is electrochemically oxidized according to

$$H_2 \rightarrow 2H^+ + 2e^- \quad (1)$$

while oxygen reduction occurs at the cathode according to

$$\frac{1}{2}O_2 + 2H^+ + 2e^- \rightarrow H_2O \quad (2)$$

The overall electrochemical reaction is therefore

$$H_2 + \frac{1}{2}O_2 \rightarrow H_2O \quad (3)$$

For a reversible electrochemical conversion process, the maximum electrical work is related to the Gibbs free-energy change in the reaction. The Gibbs free-energy change varies with operating temperature according to

$$\Delta G(T) = \Delta H - T\Delta S \quad (4)$$

where ΔH and ΔS denote the enthalpy and entropy changes in the electrochemical reaction, respectively, and (T) is the absolute operating temperature. The corresponding standard reversible potential is

$$E_0^r(T) = -\frac{\Delta G(T)}{nF} \quad (5)$$

where n is the number of electrons transferred per mole of hydrogen and F is Faraday's constant.

Under non-standard operating conditions, the reversible potential is determined from:

$$E_r(T) = E_r^0(T) + \frac{RT}{nF}\ln\left(\frac{P_{H_2}P_{O_2}^{0.5}}{P_{H_2O}}\right) \quad (6)$$

where E_r^0 is the reversible potential under standard conditions, R is the universal gas constant, and P_{H_2}, P_{O_2} and P_{H_2O} represent the respective partial pressures of hydrogen, oxygen, and water. Equations (4)–(6) show explicitly that the reversible potential is temperature dependent through both the Gibbs free-energy term and the Nernst correction. This temperature dependence was part of the electrochemical formulation used to generate the response data for the subsequent response-surface analysis. The notation has been used here to make the dependence of E_R and E_r^0 on temperature explicit; therefore, this clarification does not require modification of the existing response-surface dataset.

The actual operating voltage is lower than the reversible potential because of electrochemical and transport irreversibilities. In the present model, three principal polarization mechanisms are considered: activation, ohmic, and concentration losses. The resulting single-cell voltage is expressed as

$$E_{cell} = E_r - \eta_{act,a} - \eta_{act,c} - \eta_{ohm} - \eta_{conc,a} - \eta_{conc,c} \quad (7)$$

Activation polarization originates from the finite reaction kinetics at the anode and cathode catalyst layers. Incorporating the equivalent internal current associated with reactant crossover, the activation losses are represented by modified Tafel relations:

$$\eta_{act,a} = A_a\ln\left(\frac{i + i_l}{i_{0,a}}\right) \quad (8)$$

and

$$\eta_{act,c} = A_c\ln\left(\frac{i + i_l}{i_{0,c}}\right) \quad (9)$$

where i is the operating current density, $i_{o,a}$ and $i_{0,c}$ are the exchange current densities of the anode and cathode, respectively, and i_l represents the equivalent internal current density associated with reactant crossover. The corresponding Tafel coefficient is calculated as

$$A = \frac{RT}{n\alpha F} \tag{10}$$

where α represents the electrode charge-transfer coefficient.

The internal-current contribution associated with hydrogen crossover is represented in the adopted model as

$$i_l = \frac{2F\dot{n}_{H_2,cross}}{A_{cell}} \tag{11}$$

where $\dot{n}_{H_2,cross}$ is the molar rate of hydrogen crossing the membrane without contributing to useful external current and A_{cell} is the active cell area.

Ohmic polarization accounts for resistance to proton transport through the electrolyte and electron transport through the electrically conducting components and external circuit. The corresponding voltage loss is expressed as

$$\eta_{ohm} = i(R_e + R_i + R_c) \tag{12}$$

where R_e, R_i and R_C denote the external electrical, ionic, and internal electronic/contact resistance contributions, respectively.

At elevated current densities, depletion of reactants near the catalyst layers produces concentration polarization. The concentration losses at the anode and cathode are represented as

$$\eta_{conc,a} = -\frac{RT}{2F}\ln\left(1 - \frac{i}{i_{m,a}}\right) \tag{13}$$

and

$$\eta_{conc,c} = -\frac{RT}{4F}\ln\left(1 - \frac{i}{i_{m,c}}\right) \tag{14}$$

where $i_{m,a}$ and $i_{m,c}$ are the limiting current densities at the anode and cathode, respectively. These expressions capture the increasingly strong mass-transfer limitation as the operating current approaches the limiting-current region.

Substitution of Equations (8)–(14) into Equation (7) gives the polarization-voltage model employed to generate the response data used subsequently in the response surface analysis:

$$E_{cell} = E_r - A_a\ln\left(\frac{i + i_l}{i_{0,a}}\right) - A_c\ln\left(\frac{i + i_l}{i_{0,c}}\right) - i(R_e + R_i + R_c) + \frac{RT}{2F}\ln\left(1 - \frac{i}{i_{m,a}}\right) + \frac{RT}{4F}\ln\left(1 - \frac{i}{i_{m,c}}\right) \tag{15}$$

The corresponding areal power density is obtained from

$$P_d = iE_{cell} \tag{16}$$

where P_d is expressed in W cm^{-2} when i is expressed in A cm^{-2}. Thus, although the cell voltage generally decreases with increasing current density, power density initially increases because of the increasing current contribution before reaching a maximum and subsequently declining as polarization losses become dominant. This trade-off provides the physical basis for using polarization voltage as the primary response-surface variable and deriving power density algebraically from Equation (16). This approach preserves the physical relationship $P_d = iE_{cell}$ throughout the subsequent optimization.

For the stack considered in the present study, 84 individual cells are connected in series, with an active area of 272 cm^2 per cell. The stack current is therefore obtained as

$$I_{stack} = iA_{cell} \tag{17}$$

whereas the stack voltage is

$$V_{stack} = N_{cell}E_{cell} \tag{18}$$

and the gross electrical power generated by the HT-PEMFC stack is

$$\dot{W}_{FC} = V_{stack}I_{stack} \tag{19}$$

where N_{cell} represents the number of cells connected in series.

The fuel-cell electrical efficiency is defined on a lower-heating-value basis as the ratio of the operating cell voltage to the thermoneutral voltage:

$$\eta_{FC} = \frac{E_{cell}}{E_{th}} \tag{20}$$

For hydrogen oxidation on an LHV basis, the thermoneutral voltage adopted in this study is Eth = 1.2488 V. Accordingly, the reference operating voltage of 0.5726 V gives η_{FC} = 45.85%.

The electrical losses represented by the polarization terms in Equation (7) ultimately contribute to heat generation within the stack. Consequently, the electrochemical operating point determines both the useful electrical power generated by the HT-PEMFC and the amount of thermal energy potentially available to the downstream ORC. The formulation used to quantify this recoverable thermal output is presented in Section 2.3.

2.3. Fuel-Cell Heat Generation and Waste-Heat Recovery

During HT-PEMFC operation, only part of the chemical energy released by the hydrogen–oxygen electrochemical reaction is converted into electrical work. The remaining fraction appears primarily as thermal energy as a consequence of the entropy change associated with the electrochemical reaction and irreversible activation, ohmic, and concentration losses. Consequently, the thermal output of the fuel-cell stack is intrinsically linked to its electrochemical operating condition. For an HT-PEMFC coupled to a bottoming thermodynamic cycle, this rejected heat constitutes a potentially useful thermal-energy source rather than an unavoidable loss [28].

The thermoneutral potential corresponding to the total reaction enthalpy is expressed as

$$E_{th} = -\frac{\Delta H}{nF} \tag{21}$$

Here, E_{th} = 1.2488 V is the thermoneutral potential based on the lower heating value (LHV) of hydrogen, ΔH is the molar enthalpy change in the hydrogen oxidation reaction, n is the number of electrons transferred per mole of hydrogen, and F is Faraday's constant.

The difference between the thermoneutral voltage and the actual operating cell voltage represents the portion of the reaction energy released as heat. Accordingly, the heat-generation rate of an HT-PEMFC stack containing N_{cell} cells connected in series is represented as

$$\dot{Q}_{FC} = N_{cell}I_{stack}(E_{th} - E_{cell}) \tag{22}$$

where I_{stack} is the stack current and E_{cell} is the operating voltage of an individual cell.

Equation (22) establishes the direct electrothermal coupling between fuel-cell operation and waste-heat availability. Increasing current density increases the electrochemical reaction rate and stack current, while increasing polarization losses generally reduces cell voltage. As a result, changes in pressure, temperature, and current density affect not only the electrical performance of the HT-PEMFC but also the quantity of thermal energy potentially available for recovery.

In the integrated configuration considered in this study, heat losses between the HT-PEMFC and the ORC evaporator are neglected. Therefore, the recoverable stack heat is assumed to be transferred directly to the ORC:

$$\dot{Q}_{rec} = \dot{Q}_{FC} = \dot{Q}_{evap} \quad (23)$$

where $\dot{Q}_{rec}$ is the recoverable fuel-cell heat and $\dot{Q}_{evap}$ is the heat transferred to the ORC working fluid.

The evaporator heat-transfer rate is independently calculated from the working-fluid enthalpy rise:

$$\dot{Q}_{evap} = \dot{m}_{ORC}(h_3 - h_2) \quad (24)$$

where $\dot{m}_{ORC}$ is the ORC working-fluid mass-flow rate and h_2 and h_3 are the specific enthalpies at the evaporator inlet and outlet, respectively. The reference ORC calculations use thermophysical properties from the Reference Fluid Thermodynamic and Transport Properties (REFPROP) database of the National Institute of Standards and Technology (NIST, Gaithersburg, MD, USA). The available thermodynamic records contain the cycle boundary conditions and aggregate component results but do not include the numerical working-fluid mass-flow rate or the complete h_1–h_4 state-property table. These quantities cannot be reconstructed uniquely from the reported heat and work rates without an additional property calculation. Therefore, the ORC analysis is restricted to the available reference-case quantities reported in Table 1.

Table 1. Principal numerical parameters and sources used in the HT-PEMFC and reference ORC calculations.

Parameter	Value	Source/Basis
PBI proton conductivity, σ	0.048 S cm^{-1}	Jayakody et al. [27], measured at 160 °C
PA/PBI molar ratio	12.2	Jayakody et al. [27]
Proton diffusion coefficient	$\leq 1 \times 10^{-7}$ cm^2 s^{-1}	Estimated upper bound, Jayakody et al. [27]
Number of electrons, *n*	2	H_2/O_2 electrochemical reaction
Faraday constant, F	96,485 C mol^{-1}	Standard constant
Universal gas constant, R	8.314 J $mol^{-1}K^{-1}$	Standard constant
Number of cells, N_{cell}	84	Present stack configuration
Active area per cell	272 cm^2	Present stack configuration
HT-PEMFC pressure range	100–400 kPa	Present RSM design
HT-PEMFC temperature range	423–473 K	Present RSM design
Current-density range	0–2.45 A cm^{-2}	Present RSM design
ORC working fluid	R409A	Retained reference dataset
Condenser pressure	0.79884 MPa	Retained REFPROP-based reference case
Evaporator pressure	2 MPa	Retained reference case
State-3 temperature	433 K	Retained reference case
Pump isentropic efficiency	0.80	Adopted model assumption
Expander isentropic efficiency	0.80	Adopted model assumption
ORC thermal input	15.45 kW	Reference HT-PEMFC case

The elevated operating temperature of the HT-PEMFC is advantageous for the present thermal-integration concept because it provides rejected heat at a temperature level more suitable for downstream conversion than that available from conventional low-temperature PEMFCs [28]. The response-surface optimization described in Section 3 therefore incorporates a lower temperature constraint of 443 K. This constraint maintains an approximately 10 K temperature difference relative to the ORC evaporator outlet temperature of approximately 433 K considered in the present thermodynamic model, thereby avoiding an operating condition in which the modeled ORC working-fluid temperature would exceed the temperature of the heat source. The resulting 10 K difference represents a terminal minimum-approach constraint in the present model. However, the model does not resolve the complete hot- and cold-side temperature–heat-duty profiles required for a full pinch analysis. Accordingly, the 15.45 kW heat-transfer rate should be interpreted as an upper-bound thermal input under the adopted full-transfer assumption rather than as a pinch-validated realistically recoverable heat rate.

The RSM analysis is used to identify an electrochemically favorable HT-PEMFC operating region under the imposed thermal constraint. The subsequent ORC analysis is evaluated using the reference thermodynamic operating case for which the retained reference thermodynamic dataset is available.

2.4. ORC Configuration and Reference Working Fluid

The ORC is employed as the bottoming cycle for converting a portion of the recoverable HT-PEMFC heat into additional electrical power. As described in Section 2.1, the cycle consists of a pump, evaporator, expander, and condenser. Organic working fluids are suitable for this application because their relatively low phase-change temperatures permit power generation from thermal sources that are unsuitable for conventional steam Rankine cycles [13].

Working-fluid selection strongly affects ORC performance through its influence on evaporation and condensation characteristics, operating pressures, expander performance, and heat-exchanger temperature matching. Zeotropic mixtures are particularly relevant for finite-temperature heat sources because their temperature glide during phase change can improve thermal matching and reduce heat-transfer irreversibility [29,30]. Experimental studies have also shown that mixture composition can significantly influence operating pressure, mass flow rate, heat-transfer behavior, and net power generation [30].

The available thermodynamic dataset for the ORC was developed using R409A as the working fluid, with thermophysical properties obtained from the NIST REFPROP database [31]. R409A is therefore retained in the present study to preserve consistency with the available thermodynamic calculations. The present work does not attempt to establish a new comparative ranking of candidate working fluids because complete component-level data, including mass-flow rate, pump work, and expander work, are not available for all candidate mixtures. Accordingly, the ORC analysis reported here is restricted to the retained R409A reference case for which aggregate heat- and work-rate results are available.

The use of R409A should be interpreted strictly as a consequence of the available thermodynamic dataset rather than as a general recommendation for new ORC installations. R409A is a legacy refrigerant mixture; therefore, future working-fluid screening should consider modern low-global-warming-potential alternatives under comparable thermodynamic conditions [30].

The condenser pressure of 0.79884 MPa was retained from the available REFPROP-based thermodynamic dataset. This value is not an independently optimized design variable; it corresponds approximately to the saturation pressure of R409A at a saturated-

liquid condenser outlet temperature of 25 °C. At this pressure, the bubble- and dew-point temperatures are approximately 24.7 °C and 31.9 °C, respectively [31].

Because R409A is a zeotropic mixture, evaporation and condensation occur over a finite temperature glide. At the evaporator pressure of 2.0 MPa, the bubble- and dew-point temperatures are approximately 61.4 °C and 66.7 °C, respectively [31]. These values correspond to temperature glides of approximately 5.3 K and 7.2 K, respectively, and confirm the non-isothermal phase-change behavior of the mixture. The turbine-inlet condition (State 3) is approximately 433 K (159.9 °C), which is well above both the evaporator dew-point temperature and the reported critical temperature of R409A (approximately 106.9 °C) [31]. However, because the evaporator pressure of 2 MPa remains below the mixture critical pressure of approximately 4.69 MPa, State 3 represents a strongly superheated vapor rather than a supercritical state. Consequently, a pseudo-critical temperature is not applicable at this subcritical pressure. The turbine-inlet temperature of approximately 160 °C also represents a high-temperature condition for the HCFC-containing R409A blend. Thermal decomposition and long-term chemical stability were not included in the present thermodynamic model; therefore, the R409A results should be interpreted as a thermodynamic reference case rather than a recommendation for practical high-temperature ORC operation.

R409A exhibits a measurable temperature glide during both evaporation and condensation, which provides the thermodynamic basis for considering a zeotropic fluid in the present heat-recovery analysis. However, its use in this study is retained primarily for consistency with the available thermodynamic dataset. Its legacy HCFC composition and the high modeled turbine-inlet temperature limit its suitability as a general recommendation for new ORC installations.

2.5. Energy Formulation

The thermodynamic performance of the R409A-based ORC was evaluated using steady-state energy balances for the pump, evaporator, expander, and condenser. Net ORC power is used for the cycle-efficiency calculations. Changes in kinetic and potential energy are neglected, and pressure and external heat losses within the ORC are assumed negligible. The pump and expander isentropic efficiencies are both assumed to be 80%, consistent with the adopted reference-case assumptions. For checking the feasibility of heat rejection, cooling water is assumed to enter the condenser at 293 K (20 °C) and leave at approximately 296 K (23 °C). These temperatures remain below the R409A condensation-temperature range of approximately 24.7–31.9 °C, thereby maintaining a positive temperature difference throughout the phase-change region. The cooling-water loop itself is not included in the cycle power calculation.

2.5.1. Pump

The ORC working fluid enters the pump as saturated liquid at state 1 and is compressed to the evaporator pressure. For the actual pumping process, the required pump power is

$$\dot{W}_p = \dot{m}_{ORC}(h_2 - h_1) = \frac{\dot{m}_{ORC}(h_{2s} - h_1)}{\eta_p} \quad (25)$$

where h_{2S} is the specific enthalpy corresponding to ideal isentropic compression and η_p is the pump isentropic efficiency.

2.5.2. Evaporator

The heat supplied to the ORC evaporator is determined using Equation (24).

2.5.3. Expander

The high-pressure vapor leaving the evaporator expands from state 3 to state 4, producing shaft power. The actual expander output is calculated as

$$\dot{W}_e = \dot{m}_{ORC}(h_3 - h_4) = \dot{m}_{ORC}(h_3 - h_{4s})\eta_e \quad (26)$$

where h_{4S} is the outlet enthalpy corresponding to isentropic expansion and η_e is the expander isentropic efficiency.

2.5.4. Condenser

After leaving the expander, the working fluid rejects heat in the condenser until it returns to the saturated-liquid condition at state 1. The condenser heat-rejection rate is calculated as

$$\dot{Q}_{cond} = \dot{m}_{ORC}(h_4 - h_1) \quad (27)$$

2.5.5. ORC Net Power and Thermodynamic Performance

The net useful power generated by the ORC is obtained by subtracting the pump-power requirement from the expander output:

$$\dot{W}_{ORC,net} = \dot{W}_e - \dot{W}_p \quad (28)$$

Accordingly, the first-law or thermal efficiency of the ORC is defined as

$$\eta_{th,ORC} = \frac{\dot{W}_{ORC,net}}{\dot{Q}_{evap}} \times 100\% \quad (29)$$

2.5.6. Integrated System Power Output

The total useful electrical power produced by the thermally integrated system is calculated as

$$\dot{W}_{sys} = \dot{W}_{FC} + \dot{W}_{ORC,net} \quad (30)$$

The combined modeled electrical output is calculated as the gross HT-PEMFC stack electrical output plus the net ORC output, where the latter accounts for the ORC working-fluid pump consumption. Reactant pressurization work, the HT-PEMFC coolant-loop pump, condenser cooling-water pumping, and DC/AC conversion losses are not included in the available model. Therefore, the quantity defined by Equation (30) represents the combined electrical output before these balance-of-plant parasitic loads and should not be interpreted as the net plant electrical output.

The principal ORC component efficiencies and boundary conditions were retained from the reference thermodynamic dataset, while R409A properties were obtained using REFPROP [31]; the remaining entries in Table 2 represent the simplifying assumptions adopted in the present thermodynamic model.

Table 2. Principal assumptions adopted for the HT-PEMFC–ORC thermodynamic model.

Parameter/Assumption	Adopted Condition
System operation	Steady state
Pump isentropic efficiency, (η_p)	0.80
Expander isentropic efficiency, (η_e)	0.80
Condenser outlet condition	Saturated liquid

Table 2. *Cont.*

Parameter/Assumption	Adopted Condition
Pressure losses in ORC piping and heat exchangers	Neglected
Heat losses from HT-PEMFC to ORC evaporator	Neglected
Reactant pressurization work	Not included
HT-PEMFC coolant-loop pump power	Not included
ORC condenser cooling-water pump power	Not included
DC/AC converter losses	Not included
Changes in kinetic and potential energy	Neglected
Separate generator losses	Not explicitly modeled
Condenser cooling-water temperature	293 K inlet; 296 K outlet (adopted for heat-rejection feasibility check)

3. Response Surface Methodology and Numerical Optimization

3.1. Response-Surface Design and Model Development

Response surface methodology (RSM) was used to quantify the simultaneous effects of HT-PEMFC operating pressure, temperature, and current density on polarization voltage. The analysis was performed using Design-Expert version 13.0.5.0 (Stat-Ease, Inc., Minneapolis, MN, USA). RSM enables nonlinear and interaction effects among operating variables to be represented using a limited number of model evaluations; the present three-factor design follows the Box–Behnken framework [32]. Before applying the RSM optimization, the HT-PEMFC electrochemical model was benchmarked against published PA/PBI HT-PEMFC polarization data, as discussed in Section 4.1.

Three continuous factors were considered: operating pressure (A), cell temperature (B), and current density (C). Pressure was varied from 100 to 400 kPa, temperature from 423 to 473 K, and current density from 0 to 2.45 A cm^{-2}. These ranges define the operating domain evaluated by the underlying HT-PEMFC electrochemical model. The factor ranges are summarized in Table 3.

Table 3. Operating variables and ranges used for the response-surface analysis.

Factor	Operating Variable	Unit	Lower Level	Upper Level
A	Pressure	kPa	100	400
B	Temperature	K	423	473
C	Current density	A cm^{-2}	0	2.45

The 17-run response-surface layout comprised 12 factor combinations corresponding to the Box–Behnken structure and five repeated evaluations at the reference condition of 250 kPa, 443 K, and 1.0 A cm^{-2}. The geometric center of the investigated factor ranges is 250 kPa, 448 K, and 1.225 A cm^{-2}. Therefore, the repeated reference condition corresponds to coded coordinates of approximately A = 0, B = −0.20, and C = −0.184, rather than the exact design center (0, 0, 0). The design is consequently described as Box–Behnken-based rather than as a conventional orthogonal Box–Behnken design.

To quantify the effect of this departure from the exact center, variance inflation factors (VIFs) were calculated for all linear, interaction, and quadratic terms using the coded 17-run design matrix. The VIF values ranged from 1.000 to 1.018, with the maximum value obtained for the temperature term. The current-density term had a VIF of 1.015, while the quadratic terms ranged from approximately 1.012 to 1.013. These values indicate only a very small departure from orthogonality. The maximum VIF of 1.018 corresponds

to less than approximately 0.9% inflation in the coefficient standard error relative to an orthogonal design. For comparison, replacing the repeated reference condition with the exact center would give VIF values close to unity, with a maximum of approximately 1.006. Therefore, the use of the off-center reference condition introduces only minor collinearity and does not materially affect interpretation of the fitted coefficients within the investigated design domain.

The response values for each operating combination were generated using the HT-PEMFC electrochemical model described in Section 2.2 and subsequently imported into Design-Expert for regression, statistical analysis, and numerical optimization. Polarization voltage was treated as the primary response for response-surface modeling. Power density was not fitted as an independent response; instead, it was calculated directly from the predicted polarization voltage and current density using Equation (16), thereby preserving the exact algebraic relationship between voltage, current density, and power density. The complete 17-run design matrix and corresponding model-generated response values are presented in Table 4.

Table 4. Box–Behnken-based response-surface design matrix and corresponding HT-PEMFC responses.

Run	Pressure (kPa)	Temperature (K)	Current Density (A cm^{-2})	Polarization Voltage (V)	Power Density (W cm^{-2})
1	250	423	2.450	0.1554	0.3806
2	250	443	1.000	0.5726	0.5726
3	100	448	2.450	0.0196	0.0480
4	400	473	1.225	0.5353	0.6558
5	250	443	1.000	0.5726	0.5726
6	250	443	1.000	0.5726	0.5726
7	400	448	0.000	1.2782	0.0000
8	400	448	2.450	0.1757	0.4304
9	250	443	1.000	0.5726	0.5726
10	250	423	0.000	1.2706	0.0000
11	100	473	1.225	0.3705	0.4539
12	250	473	2.450	0.0900	0.2209
13	100	423	1.225	0.4393	0.5382
14	100	448	0.000	1.2648	0.0000
15	250	473	0.000	1.2766	0.0000
16	400	423	1.225	0.5867	0.7187
17	250	443	1.000	0.5726	0.5726

A second-order polynomial was fitted to the polarization-voltage response to represent the combined linear, interaction, and quadratic effects of the three operating variables.

$$Y = \beta_0 + \beta_A A + \beta_B B + \beta_C C + \beta_{AB} AB + \beta_{AC} AC + \beta_{BC} BC + \beta_{AA} A^2 + \beta_{BB} B^2 + \beta_{CC} C^2 \quad (31)$$

where Y represents polarization voltage response, β_0 is the intercept, β_A, β_B, and β_C are the linear regression coefficients, β_{AB}, β_{AC}, and β_{BC} represent two-factor interaction effects, and β_{AA}, β_{BB}, and β_{CC} represent quadratic effects.

Goodness-of-fit statistics, regression diagnostics, and coded-coefficient effect magnitudes were used to evaluate model adequacy and interpret the relative influence of the operating variables. The fitted polarization-voltage model was subsequently used for physically consistent constrained optimization. Although the models were developed over the complete ranges listed in Table 3, the optimization temperature was restricted to 443–473 K to maintain a positive thermal margin relative to the approximately 433 K ORC evaporator outlet, and the minimum polarization voltage was constrained to 0.50 V. The complete optimization criteria are given in Section 3.3.

3.2. Model Adequacy and Standardized Effect Magnitudes

The quadratic polarization-voltage model was evaluated using goodness-of-fit statistics, regression diagnostics, and the magnitudes of the coefficients in coded-factor form. Because the response values were generated deterministically from the electrochemical model rather than obtained from independent physical experiments, conventional inferential *p*-values were not used to classify individual model terms as statistically significant. The repeated reference evaluations likewise do not represent independent experimental replicates and were therefore not interpreted as a source of experimental pure error.

Since pressure, temperature, and current density were expressed as coded factors on comparable scales, the magnitudes of the coded regression coefficients provide a direct descriptive measure of the relative strength of the linear, interaction, and quadratic effects. To facilitate comparison, the relative contribution of each term was calculated as its absolute coded-coefficient magnitude divided by the sum of the absolute magnitudes of all coded coefficients, multiplied by 100. These percentages are used only as descriptive effect measures and should not be interpreted as a formal decomposition of variance.

Polarization-Voltage Model

The standardized effect magnitudes for the polarization-voltage model are presented in Table 5. Current density produced the strongest effect within the investigated domain. Its linear term accounted for approximately 59.6% of the normalized absolute coefficient magnitude, while the quadratic current-density term contributed a further 22.8%, confirming the strongly nonlinear dependence of polarization voltage on electrochemical loading. Pressure showed a smaller positive contribution of approximately 6.2%, whereas the direct temperature contribution was approximately 2.3%. Among the interaction terms, the pressure–current-density interaction was the strongest, with a relative contribution of approximately 3.7%.

Table 5. Coded coefficients, normalized relative effect magnitudes, and variance inflation factors for the polarization-voltage model.

Model Term	Coded Coefficient	Direction	Relative Contribution (%)	VIF
A—Pressure	+0.0601	+	6.2	1.000
B—Temperature	−0.0224	−	2.3	1.018
C—Current density	−0.5812	−	59.6	1.015
AB	+0.0043	+	0.4	1.000
AC	+0.0357	+	3.7	1.000
BC	−0.0179	−	1.8	1.001
A^2	+0.0091	+	0.9	1.013
B^2	+0.0226	+	2.3	1.012
C^2	+0.2219	+	22.8	1.012

These values are interpreted as descriptive effect magnitudes rather than inferential statistical measures. In particular, no claim of statistical significance is made because the response values originate from deterministic electrochemical-model evaluations rather than independent experimental observations.

Current density (C) was the dominant linear effect, followed by pressure (A) and temperature (B). Among the interaction terms, AC had the largest coded-coefficient magnitude, whereas AB and BC were comparatively small. Among the quadratic terms, C^2 showed the strongest contribution, confirming the pronounced nonlinear dependence of polarization voltage on current density.

The fitted quadratic equation in terms of coded factors is

$$\begin{aligned}\text{Polarization Voltage} = {} & +0.4536 + 0.0601A - 0.0224B - 0.5812C + 0.0043AB \\ & +0.0357AC - 0.0179BC + 0.0091A^2 + 0.0226B^2 + 0.2219C^2\end{aligned} \quad (32)$$

Because Equation (32) is expressed in coded factors, the magnitudes and signs of the coefficients indicate the relative direction and strength of factor effects within the investigated design domain. The large negative coefficient of C reflects the reduction in polarization voltage with increasing current density, whereas the positive coefficient of A indicates improved voltage performance at higher pressure.

The polarization-voltage surrogate showed close agreement with the model-generated response data, with R^2 = 0.9989, adjusted R^2 = 0.9974, and predicted R^2 = 0.9819. The residual standard deviation was 0.0215 V and the coefficient of variation was 3.55%. These goodness-of-fit measures, together with the predicted-versus-generated comparison in Figure 2, were used to assess the suitability of the surrogate for response interpretation and constrained optimization.

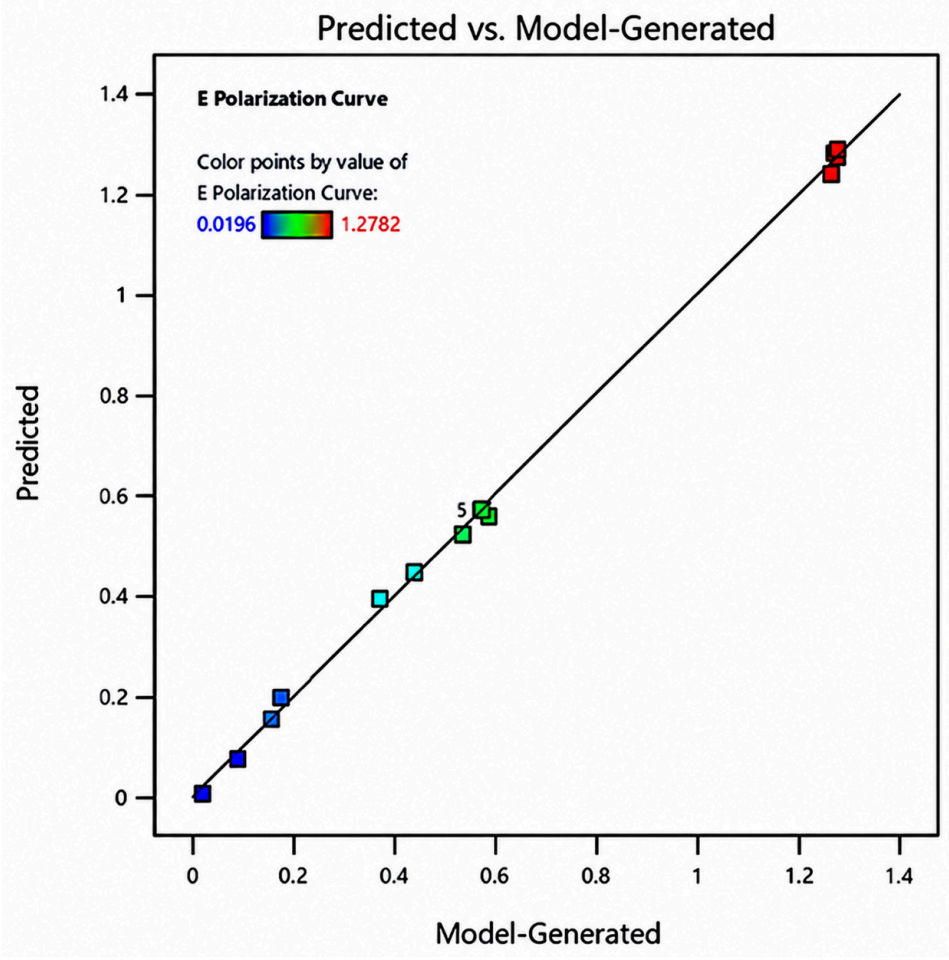


Figure 2. Predicted versus model-generated polarization-voltage values for the quadratic response-surface model.

Figure 2 compares the quadratic-model predictions with the model-generated response values. The data points are closely distributed around the equality line, consistent with the high coefficients of determination.

3.3. Physically Consistent Constrained Optimization

Following fitting and adequacy assessment of the polarization-voltage response surface, power density was calculated directly from the predicted voltage rather than represented by a separate independently fitted response surface. The predicted power density was therefore obtained as

$$\hat{P}_d = i\hat{E} \tag{33}$$

where $\hat{E}$ is the polarization voltage predicted by Equation (32). This formulation guarantees algebraic consistency between current density, polarization voltage, and power density throughout the optimization.

The objective of the numerical optimization was to maximize the physically consistent power density defined by Equation (33), subject to the investigated ranges of pressure, temperature, and current density. In addition, the minimum temperature was restricted to 443 K to maintain an approximately 10 K thermal margin relative to the ORC evaporator outlet temperature of approximately 433 K, while the minimum allowable polarization voltage was set to 0.50 V to avoid excessively low-voltage operation.

For a fixed pressure and temperature, the stationary power-density condition can be expressed as

$$\frac{\partial \hat{P}_d}{\partial i} = \hat{E} + i\frac{\partial \hat{E}}{\partial i} = 0 \tag{34}$$

The constrained search showed that the maximum physically consistent power density occurs at the upper investigated pressure boundary of 400 kPa and the lower thermally allowable temperature of 443 K. Substitution of these conditions into Equation (32) gives the voltage response as a function of current density:

$$\hat{E} = 1.291144 - 0.804669i + 0.147872i^2 \tag{35}$$

Accordingly,

$$\hat{P}_d = 1.291144i - 0.804669i^2 + 0.147872i^3 \tag{36}$$

Application of Equation (34) gives a physically relevant stationary point at approximately i = 1.198 A cm^{-2}. At this condition, the response-surface model predicts a polarization voltage of approximately 0.5395 V, giving a power density of approximately 0.6462 W cm^{-2} from Equation (33). The voltage therefore remains above the imposed minimum of 0.50 V.

The optimization also clarifies the role of the individual constraints. Within the investigated response-surface domain, increasing pressure improves the predicted voltage and derived power density, while the thermal-integration requirement restricts the temperature to values of 443 K or higher. Consequently, the optimum occurs at the upper pressure boundary of 400 kPa and the lower permitted temperature boundary of 443 K rather than at an interior pressure–temperature combination. The optimum current density is not determined by the minimum-voltage constraint. Instead, it is obtained from the stationary condition of the physically consistent power-density function, giving approximately 1.198 A cm^{-2}, at which the predicted voltage remains above the imposed minimum at approximately 0.5395 V.

Accordingly, the main contribution of the response-surface model is not the identification of an unexpected interior optimum in pressure and temperature. Its value lies in providing a compact quantitative representation of the nonlinear polarization response and the interaction effects among pressure, temperature, and current density, from which a physically consistent power-density function can be derived and optimized. The boundary

nature of the pressure and temperature solution is therefore stated explicitly and should be interpreted within the investigated operating ranges.

The constrained search was performed using the criteria listed in Table 6, and the feasible condition giving the maximum physically consistent power density was selected. The resulting constrained optimum and its comparison with the reference operating condition are presented and discussed in Section 4.3.

Table 6. Constraints used for physically consistent HT-PEMFC optimization.

Variable/Response	Constraint
Pressure, (A)	100–400 kPa
Temperature, (B)	443–473 K
Current density, (C)	0–2.45 A cm^{-2}
Polarization voltage, $(\hat{E})$	$E \geq 0.50$ V
Power density, $(\hat{P}_d)$	Maximize $\hat{P}_d = i\hat{E}$

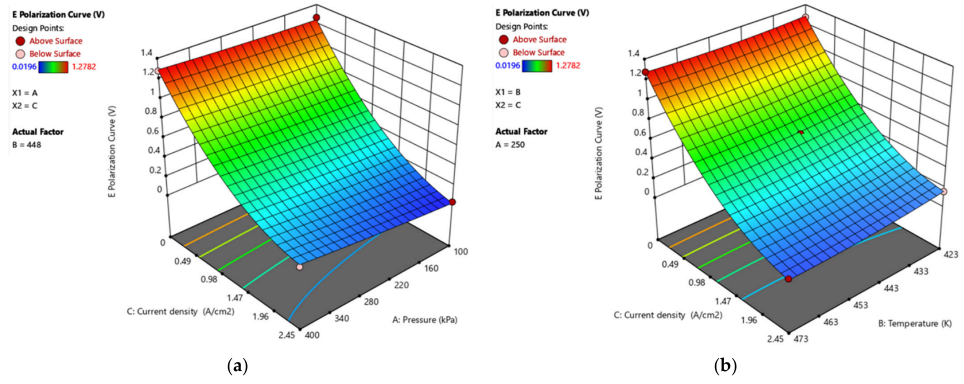
4. Results and Discussion

4.1. Effects of Operating Parameters on Polarization Voltage

The response-surface analysis shows that polarization voltage is influenced primarily by current density, while pressure provides a secondary beneficial effect and temperature has a comparatively smaller influence. This trend is consistent with the statistical analysis presented in Section 3.2, which identified current density as the dominant factor affecting the polarization response.

Across the investigated operating range, polarization voltage decreased markedly as current density increased. At 400 kPa and 448 K, for example, the voltage decreased from 1.2782 V at zero current density to 0.1757 V at 2.45 A cm^{-2}. At 100 kPa and the same temperature, the corresponding voltage at 2.45 A cm^{-2} was only 0.0196 V. The strong decline at high current density reflects the increasing contribution of activation, ohmic, and mass-transfer losses.

Pressure generally improved polarization performance, particularly at elevated current density. As shown in Figure 3a, increasing pressure from 100 to 400 kPa had only a small effect near open-circuit conditions but produced a substantially larger improvement at high current density. This behavior is consistent with improved reactant availability and reduced sensitivity to transport limitations under elevated-pressure operation [24].



(**a**) (**b**)

Figure 3. Response-surface effects of HT-PEMFC operating parameters on polarization voltage: (**a**) interaction between pressure and current density at 448 K; (**b**) interaction between temperature and current density at 250 kPa.

The effect of temperature was dependent on the electrochemical loading condition rather than being uniformly positive or negative throughout the investigated domain. At

zero current density and 250 kPa, increasing the temperature from 423 to 473 K changed the predicted voltage only slightly, from 1.2706 to 1.2766 V. In contrast, at 2.45 A cm^{-2} and the same pressure, increasing the temperature from 423 to 473 K reduced the predicted voltage from 0.1554 to 0.0900 V. The negative temperature effect at high current density differs from the generally beneficial effect of increasing temperature reported in experimental HT-PEMFC studies, where improved reaction kinetics can enhance performance [24,25]. Chowdhury and Gladen [24], for example, identified temperature as an important operating parameter, while Zhou et al. [25] showed that higher temperature can mitigate performance losses under diluted-anode operation.

The difference should be interpreted in the context of the present electrochemical formulation. Temperature enters not only the reversible-potential relation in Equations (4)–(6), but also the activation and concentration overpotentials through the RT/F-dependent terms in Equations (8)–(10), (13) and (14). At elevated current density, these polarization terms become increasingly important and produce the negative temperature dependence predicted by the adopted model. In addition, the present model uses the adopted membrane-conductivity parameter without a separate temperature-dependent conductivity correlation and does not include explicit temperature-dependent degradation phenomena. Therefore, the predicted negative trend at high current density should be regarded as a model-specific electrochemical response rather than evidence of phosphoric-acid evaporation, membrane dry-out, or other degradation mechanisms. Such mechanisms are outside the scope of the present model.

The response surfaces therefore confirm that current density is the principal control variable for polarization voltage, while increased pressure partly mitigates voltage deterioration under high-current operation. Because maximum voltage occurs close to open circuit, where useful power output approaches zero, polarization voltage was treated as a constrained response rather than a maximization objective during numerical optimization.

To provide an external literature comparison, the model-predicted polarization curve at 433 K and 100 kPa was compared with published PA/PBI HT-PEMFC experimental data digitized from Zhang et al. [33] measured at 160 °C, ambient backpressure, and 0% RH (see Figure 4). The comparison shows the overall decreasing polarization trend, although quantitative deviations remain, with a root-mean-square error (RMSE) of 0.230 V. It should be noted that the published data were digitized from the reported figure and that some deviation is expected due to differences in membrane properties, MEA structure, and detailed operating conditions.

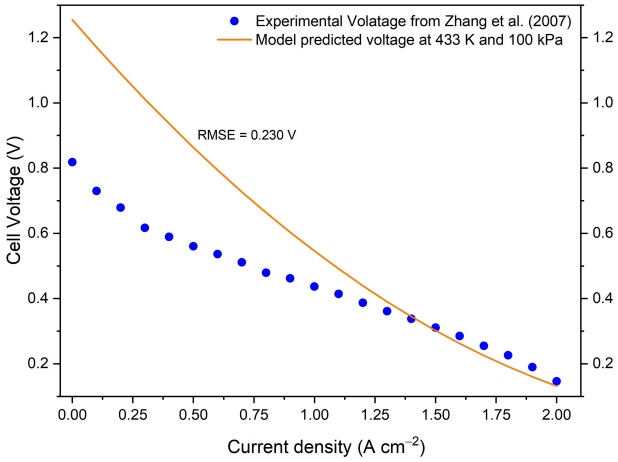
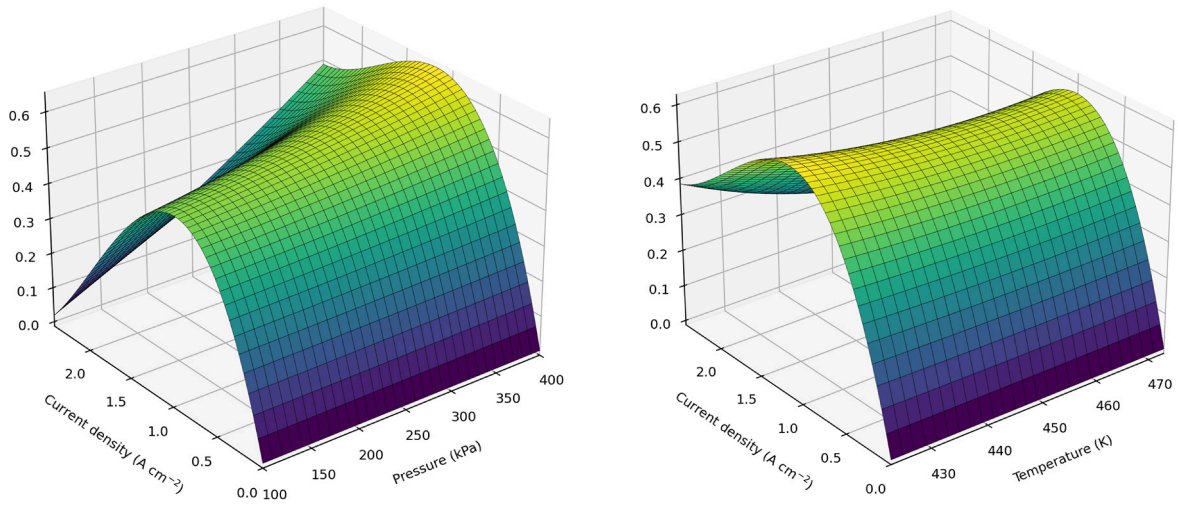


Figure 4. Comparison between the model-predicted polarization curve and the published experimental PA/PBI HT-PEMFC data digitized from Zhang et al. [33] at 160 °C (433 K), ambient backpressure, and 0% RH.

4.2. Effects of Operating Parameters on Power Density

Power density exhibited a strongly nonlinear dependence on current density. Unlike polarization voltage, which decreased continuously with increasing current density, power density initially increased from zero, reached a maximum within an intermediate current-density region, and subsequently declined as polarization losses became dominant. This behavior is consistent with the strong quadratic current-density effect identified in Section 3.2.

Pressure had a clear beneficial influence on power density, particularly at moderate-to-high current density. Figure 5a shows the combined effect of pressure and current density at 448 K. At 2.45 A cm^{-2}, increasing pressure from 100 to 400 kPa raised the model-generated power density from 0.0480 to 0.4304 W cm^{-2}. The improvement is consistent with the corresponding polarization response, where increased pressure helped maintain a higher operating voltage under elevated electrochemical loading [24].



(**a**) (**b**)

Figure 5. Physically consistent power-density surfaces derived from the RSM-predicted polarization voltage using P_d = iE: (**a**) effect of pressure and current density at 448 K; (**b**) effect of temperature and current density at 250 kPa. In both panels, the color gradient represents power density, progressing from lower values (purple/blue) to higher values (yellow).

A similar pressure effect was observed at intermediate current density. At approximately 1.23 A cm^{-2} and 423 K, increasing pressure from 100 to 400 kPa increased power density from 0.5382 to 0.7187 W cm^{-2}. This behavior explains why the numerical optimization favored the upper-pressure region of the investigated design space.

Temperature showed a smaller but noticeable influence on power density. Figure 5b illustrates the interaction between temperature and current density at a fixed pressure of 250 kPa. Separately, the design-run results at 400 kPa show that at approximately 1.23 A cm^{-2}, increasing temperature from 423 to 473 K reduced power density from 0.7187 to 0.6558 W cm^{-2}. Within the present model, lower temperatures in the investigated HT-PEMFC range therefore favored power density. This negative high-current-density trend is consistent with the polarization-voltage behavior discussed in Section 4.1 and results from the combined temperature dependence represented by the reversible-potential, activation, and concentration-polarization terms of the adopted model. Because phosphoric-acid evaporation, membrane dry-out, and temperature-dependent degradation are not explicitly modeled, the result should not be interpreted as evidence of these mechanisms.

The highest power density among the 17 response-surface design runs was 0.7187 W cm^{-2}, obtained at 400 kPa, 423 K, and approximately 1.23 A cm^{-2}. However, this condition was not suitable for the thermally integrated configuration because 423 K is below the 443 K minimum imposed to preserve an adequate temperature difference relative to the approximately 433 K ORC evaporator outlet. The numerical optimization therefore represents a compromise between high electrical performance, acceptable polarization voltage, and the temperature requirement imposed by downstream heat recovery.

4.3. Constrained RSM Optimum and Reference Operating Point

Using the physically consistent formulation in Equation (33), the constrained optimization identified an HT-PEMFC operating condition of approximately 400 kPa, 443 K, and 1.198 A cm^{-2}. At this condition, Equation (32) predicts a polarization voltage of approximately 0.5395 V. The corresponding power density, calculated directly as $P_d = iE$, is approximately 0.6462 W cm^{-2}. The optimization therefore satisfies the electrochemical identity directly.

The selected operating condition satisfies both integration constraints: the polarization voltage remains above the imposed minimum of 0.50 V, while the temperature of 443 K provides the prescribed approximately 10 K thermal margin relative to the ORC evaporator outlet temperature of approximately 433 K. The optimum occurs at the upper investigated pressure boundary and the lower thermally allowable temperature boundary and should therefore be interpreted as a constrained optimum within the investigated design domain. The reference condition of 250 kPa, 443 K, and 1.0 A cm^{-2} was retained as the baseline because it is the operating point for which the retained reference thermodynamic dataset is available; it is not intended to represent a manufacturer-specified or globally optimal operating point.

The optimized condition was compared with the reference operating point of 250 kPa, 443 K, and 1.0 A cm^{-2}. At the reference condition, the polarization voltage and corresponding power density are both approximately 0.5726 in their respective units. The comparison is summarized in Table 7. The corresponding model-implied reversible (Nernst) potentials, obtained from the zero-current limit of the fitted polarization-voltage surface at the same pressure and temperature conditions, are approximately 1.2585 V for the reference condition and 1.2911 V for the optimum.

Table 7. Comparison between the reference HT-PEMFC operating condition and the constrained RSM optimum.

Parameter	Reference Condition	Constrained Optimum	Change
Pressure	250 kPa	400 kPa	+60.0%
Temperature	443 K	443 K	–
Current density	1.000 A cm^{-2}	1.198 A cm^{-2}	+19.8%
Polarization voltage	0.5726 V	0.5395 V	−5.8%
Power density	0.5726 W cm^{-2}	0.6462 W cm^{-2}	+12.9%

The physically consistent optimum therefore provides an approximately 12.9% increase in power density relative to the reference operating point, while the polarization voltage decreases by only approximately 5.8%. The result preserves the fundamental relationship $P_d = iE$ and therefore provides a physically consistent basis for interpretation and optimization.

The optimized electrochemical condition is used only to identify an improved HT-PEMFC operating region. The subsequent stack-heat and ORC calculations continue to use

the separate reference thermodynamic case for which the retained reference thermodynamic dataset is available. No new ORC state properties are inferred from the RSM optimum.

The solution should be interpreted as a boundary-constrained optimum rather than an interior optimum in all three operating variables. Pressure reaches the upper investigated limit of 400 kPa because higher pressure consistently improves the predicted electrochemical performance within the modeled domain. Temperature remains at the lower permitted value of 443 K because lower temperatures favor the derived power density within the present model, while 443 K is the minimum value allowed by the downstream ORC thermal requirement. The current density behaves differently: it is not located at a prescribed boundary or at the minimum-voltage constraint, but is determined by the stationary maximum of $P_d = iE$, giving approximately 1.198 A cm^{-2}. At this point, the predicted voltage is approximately 0.5395 V and therefore the $E \geq 0.50$ constraint is inactive.

These results show that the principal information provided by the RSM is the quantitative description of the voltage response, including interaction and nonlinear effects, rather than the discovery of an interior optimum for pressure and temperature. The resulting surrogate allows the power-density optimum with respect to current density to be determined consistently while clearly identifying the pressure and temperature boundaries favored by the adopted model and constraints.

4.4. HT-PEMFC Stack Power, Heat Generation, and Efficiency

The electrical and thermal characteristics of the HT-PEMFC were evaluated using the reference thermodynamic operating case for which the retained reference thermodynamic dataset is available. This case corresponds to a current density of 1.0 A cm^{-2}, an active cell area of 272 cm^2, and 84 cells connected in series. The resulting stack current is 272 A, while the single-cell voltage of approximately 0.5726 V gives a stack voltage of approximately 48.1 V and an electrical output of 13.08 kW.

Figure 6 shows the variation in stack electrical power and thermal output with current. Electrical power initially increases with current, but the rate of increase progressively decreases as activation, ohmic, and concentration losses reduce the operating voltage. In contrast, thermal output increases as the difference between the thermoneutral and actual cell potentials becomes larger.

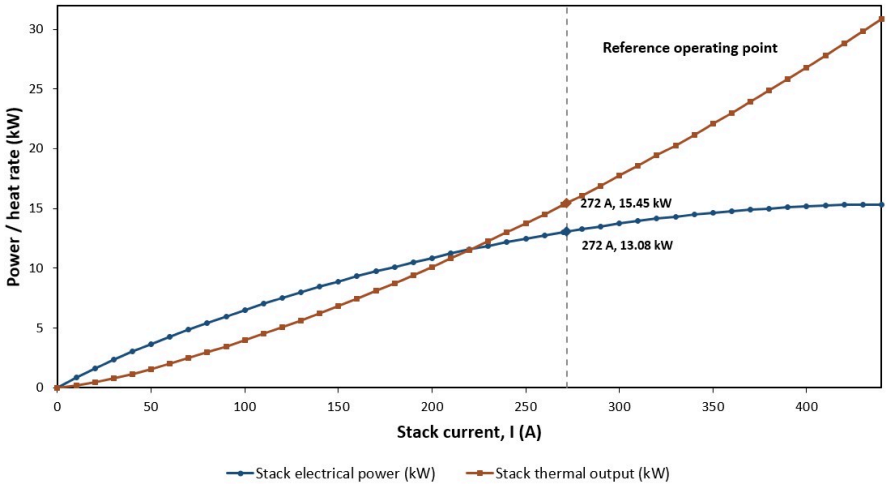


Figure 6. Variation in HT-PEMFC stack electrical power and thermal output with stack current. The vertical dashed line denotes the reference stack current of 272 A; the markers indicate the corresponding reference thermodynamic operating point.

At the reference stack current of 272 A, the model predicts 13.08 kW of electrical power and 15.45 kW of stack thermal output assumed available to the ORC. The corresponding

HT-PEMFC efficiency is 45.85%. The substantial thermal output available at this operating condition provides the heat source for the R409A-based ORC considered in the following subsection. The elevated operating temperature of the HT-PEMFC is advantageous in this respect because it provides rejected heat at a more useful temperature level for downstream thermal conversion [28].

4.5. ORC Performance at the Reference Operating Condition

The R409A-based ORC was evaluated using the 15.45 kW thermal input assumed available from the HT-PEMFC reference operating case. The ORC operates between a condenser pressure of 0.79884 MPa and an evaporator pressure of 2 MPa and receives 15.45 kW of thermal energy from the HT-PEMFC. At this condition, the expander produces 1.304 kW of power, while the pump requires 0.0654 kW. Therefore, according to Equation (28), the net ORC power is approximately 1.239 kW. Using Equation (29), the corresponding net cycle efficiency is

$$\eta_{th,ORC} = \frac{1.304 - 0.0654}{15.45} \times 100 \approx 8.02\%$$

Although the ORC output is considerably smaller than the primary HT-PEMFC electrical output, it is obtained from thermal energy that would otherwise be rejected. The cycle therefore increases useful energy recovery without requiring an additional primary fuel input.

4.6. Integrated HT-PEMFC–ORC Performance

The HT-PEMFC produces 13.08 kW of gross stack electrical power. The ORC expander produces 1.304 kW, while its working-fluid pump consumes 0.0654 kW, giving an ORC net contribution of approximately 1.24 kW. The resulting combined modeled electrical output is approximately 14.32 kW before balance-of-plant parasitic loads. The ORC contribution is equivalent to approximately 9.5% of the gross HT-PEMFC stack electrical output. Because reactant pressurization, coolant pumping, condenser cooling-water pumping, and DC/AC conversion losses are not included, this value should not be interpreted as a 9.5% increase in net plant electrical output.

Zhou et al. [20] reported a 1.65% increase in system electrical efficiency for their PEMFC–ORC configuration. In the present study, the approximately 9.5% value represents the ratio of the ORC net power contribution to the gross HT-PEMFC stack electrical output. The two percentages therefore represent different performance metrics and system boundaries and are not directly comparable.

The principal thermodynamic results of the reference integrated system are summarized in Table 8.

Table 8. Thermodynamic performance of the reference integrated HT-PEMFC–ORC system.

Performance Parameter	Value
HT-PEMFC gross stack electrical output	13.08 kW
HT-PEMFC thermal input assumed available to the ORC	15.45 kW
HT-PEMFC electrical efficiency (LHV basis)	45.85%
ORC evaporator pressure (reference case)	2 MPa
ORC gross expander output	1.304 kW
ORC working-fluid pump consumption	0.0654 kW
ORC net electrical contribution	≈1.24 kW
Net ORC thermal efficiency	≈8.02%
Combined modeled electrical output before balance-of-plant (BOP) auxiliary power consumption	≈14.32 kW
ORC contribution relative to gross HT-PEMFC stack output	≈9.5%

The additional ORC contribution is modest relative to the primary fuel-cell output; however, its thermodynamic value arises from recovering energy that would otherwise be rejected to the surroundings. Similar benefits have been reported for PEMFC–ORC configurations in which bottoming cycles improve the utilization of fuel-cell energy streams.

The integrated thermodynamic results reported here correspond to the reference thermodynamic operating case, whereas the constrained RSM optimum discussed in Section 4.3 represents the optimized electrochemical operating region. The two analyses therefore demonstrate complementary improvement strategies: optimization of HT-PEMFC operating conditions and recovery of available stack waste heat through the ORC.

5. Conclusions

This study investigated the thermodynamic integration of an HT-PEMFC with an ORC for recovery of low-grade fuel-cell waste heat, while RSM was employed to examine and optimize the electrochemical operating conditions of the HT-PEMFC. The analysis considered pressure, temperature, and current density as the principal operating variables affecting polarization voltage and power density. The response-surface results showed that current density was the dominant parameter governing polarization voltage and, through the relation $P_d = iE$, strongly influenced the derived power density, while pressure provided a notable beneficial effect, particularly at moderate-to-high current densities.

The physically consistent optimization identified an operating condition of approximately 400 kPa, 443 K, and 1.198 A cm^{-2}. At this condition, the voltage response-surface model predicted approximately 0.5395 V, corresponding to a power density of approximately 0.6462 W cm^{-2} when calculated directly from $P_d = iE$. Compared with the reference condition of 250 kPa, 443 K, and 1.0 A cm^{-2}, this represents an approximately 12.9% increase in power density. Deriving power density directly from the voltage response ensures algebraic consistency and avoids the deviation produced when the two quantities are fitted independently. The optimum lies at the upper pressure and lower permitted temperature boundaries of the investigated domain, whereas the optimum current density is determined by the stationary maximum of the physically consistent $P_d = iE$ relation rather than by the minimum-voltage constraint.

For the thermodynamic reference case, the 84-cell HT-PEMFC stack produced 13.08 kW of electrical power and approximately 15.45 kW of stack thermal output assumed available to the ORC at a stack current of 272 A. The available thermodynamic reference case employed R409A as the ORC working fluid and was therefore retained for the waste-heat-recovery analysis. At the reference evaporator pressure of 2 MPa, the ORC expander produced 1.304 kW, while the pump consumed 65.4 W.

For the reference thermodynamic case, the ORC provided approximately 1.24 kW of cycle-net power, corresponding to about 9.5% of the gross HT-PEMFC stack electrical output. The resulting combined modeled output was approximately 14.32 kW before unmodeled balance-of-plant auxiliary power consumption.

An important limitation of the present analysis is that the identified RSM optimum was not propagated through the complete ORC thermodynamic model because corresponding heat-generation and ORC state-property data were unavailable. Accordingly, the RSM optimum represents the improved electrochemical operating condition, whereas the ORC performance corresponds to the available reference thermodynamic operating case. The optimized operating point should be interpreted within the specific model structure and investigated design space rather than as a universally applicable HT-PEMFC operating condition. The results depend on the adopted PA/PBI membrane properties, the selected pressure–temperature–current-density ranges, the simplified electrochemical formulation, and the retained R409A-based ORC reference dataset. In addition, balance-of-plant auxil-

iary consumption, detailed pinch-based heat-exchanger design, temperature-dependent degradation, and broader working-fluid screening were not included. The reported ORC efficiency of approximately 8.02% is specific to the retained legacy R409A reference case and should not be interpreted as the optimum attainable with modern working fluids selected for this temperature range.

Future work should evaluate the complete integrated cycle at the optimized HT-PEMFC operating point, experimentally validate the electrochemical and thermal predictions, and incorporate temperature-dependent membrane conductivity, kinetic parameters, and phosphoric-acid transport or degradation effects. The ORC analysis should also be extended to modern low-global-warming-potential working fluids, detailed heat-exchanger matching, and complete auxiliary-power modeling.

Author Contributions: Conceptualization, F.A. and A.A.Z.; methodology, A.J. and A.A.Z.; software, A.A.Z. and A.J.; validation, F.A., F.J.A. and A.H.; formal analysis, A.A.Z., F.A. and A.H.; investigation, F.J.A. and A.J.; resources, A.H. and A.A.Z.; data curation, A.J. and F.J.A.; writing—original draft preparation, F.A., A.J. and A.A.Z.; writing—review and editing, A.H., A.A.Z. and F.J.A.; visualization, A.J. and F.J.A.; supervision, A.H.; project administration, F.A. and A.H.; funding acquisition, A.H. All authors have read and agreed to the published version of the manuscript.

Funding: This work was funded by the Deanship of Scientific Research (DSR) at King Abdulaziz University, Jeddah, Saudi Arabia, under grant IPP: 686-829-2026. The authors, therefore, acknowledge with thanks DSR for technical and financial support.

Data Availability Statement: The original contributions presented in this study are included in the article. Further inquiries can be directed to the corresponding authors.

Acknowledgments: The authors gratefully acknowledge the Deanship of Scientific Research (DSR) at King Abdulaziz University, Jeddah, Saudi Arabia, for funding this project under grant No. (IPP: 686-829-2026) and for providing technical support. During the preparation of this manuscript, the authors used Gemini (Gemini 3.1 Pro, Google LLC, Mountain View, CA, USA) to generate the schematic presented in Figure 1 based on author-provided instructions. The authors reviewed, edited, and verified the generated output and take full responsibility for the accuracy, originality, integrity, and final content of Figure 1 and this publication. To the best of the authors' knowledge, the final figure does not reproduce any third-party copyrighted graphical material.

Conflicts of Interest: The authors declare no conflicts of interest.

Abbreviations

The following abbreviations are used in this manuscript:

AC	Alternating current
DC	Direct current
HT-PEMFC	High-temperature proton-exchange membrane fuel cell
NIST	National Institute of Standards and Technology
ORC	Organic Rankine cycle
PBI	Polybenzimidazole
PEMFC	Proton-exchange membrane fuel cell
REFPROP	Reference Fluid Thermodynamic and Transport Properties
RSM	Response surface methodology
HCFC	Hydrochlorofluorocarbon
LHV	Lower heating value
PA	Phosphoric acid
RH	Relative humidity
RMSE	Root-mean-square error
VIF	Variance inflation factor

Symbols for HT-PEMFC electrochemical model:

Symbol	Definition	Unit
A	Tafel coefficient, Equation (10)	V
A_a	Anode Tafel coefficient	V
A_c	Cathode Tafel coefficient	V
A_{Cell}	Active area of a single fuel cell	cm^2
E_{Cell}	Operating voltage of a single fuel cell	V
E_r	Reversible cell potential	V
E_r^0	Reversible potential under standard conditions	V
Eth	Thermoneutral voltage	V
F	Faraday constant	C mol^{-1}
i	Operating current density	A cm^{-2}
i_l	Equivalent internal current density associated with hydrogen crossover	A cm^{-2}
$i_{0,a}$	Anode exchange current density	A cm^{-2}
$i_{0,c}$	Cathode exchange current density	A cm^{-2}
$i_{m,a}$	Anode limiting current density	A cm^{-2}
$i_{m,c}$	Cathode limiting current density	A cm^{-2}
I_{stack}	Stack current	A
n	Number of electrons transferred per mole of hydrogen	–
$\dot{n}_{H_2,Cross}$	Molar rate of hydrogen crossover	mol s^{-1}
N_{cell}	Number of cells connected in series	–
P_{H_2}	Hydrogen partial pressure	Consistent pressure basis
P_{O_2}	Oxygen partial pressure	Consistent pressure basis
P_{H_2O}	Water partial pressure	Consistent pressure basis
σ	PBI proton conductivity	S cm^{-1}
P_d	Areal power density	W cm^{-2}
R	Universal gas constant	J mol^{-1} K^{-1}
R_e	External electrical resistance contribution	Ω cm^2 *
R_i	onic resistance contribution	Ω cm^2 *
R_c	Internal electronic/contact resistance contribution	Ω cm^2 *
T	Absolute operating temperature	K
V_{stack}	HT-PEMFC stack voltage	V
$\dot{W}_{FC}$	HT-PEMFC stack electrical power	kW
α	Electrode charge-transfer coefficient	–
ΔG	Gibbs free-energy change in reaction	J mol^{-1}
ΔH	Enthalpy change in reaction	J mol^{-1}
ΔS	Entropy change in reaction	mol^{-1} K^{-1}
$\eta_{act,a}$	Anode activation overpotential	V
$\eta_{act,c}$	Cathode activation overpotential	V
η_{ohm}	Ohmic overpotential	V
$\eta_{conc,a}$	Anode concentration overpotential	V
$\eta_{conc,c}$	Cathode concentration overpotential	V
η_{FC}	HT-PEMFC electrical efficiency on an LHV basis	% or dimensionless

* For R_e, R_i, and R_c, Ω cm^2 is implied by Equation (12) because these terms are multiplied by current density in A cm^{-2} to produce a voltage loss.

Symbols for heat recovery and ORC model

Symbol	Definition	Unit
$\dot{Q}_{FC}$	HT-PEMFC heat-generation rate	kW
$\dot{Q}_{rec}$	Recoverable HT-PEMFC heat rate	kW

$\dot{Q}_{evap}$	Heat-transfer rate in the ORC evaporator	kW
$\dot{Q}_{cond}$	Heat-rejection rate in the condenser	kW
$\dot{m}_{ORC}$	ORC working-fluid mass-flow rate	kg s^{-1}
h_1, h_2, h_3, h_4	Specific enthalpies at ORC states 1–4	kJ kg^{-1}
h_{2s}	Specific enthalpy after isentropic pump compression	kJ kg^{-1}
h_{4s}	Specific enthalpy after isentropic expansion	kJ kg^{-1}
$\dot{W}_P$	ORC pump power consumption	kW
$\dot{W}_e$	ORC expander power output	kW
$\dot{W}_{ORC,net}$	Net ORC power output	kW
$\dot{W}_{sys}$	Total integrated-system electrical output	kW
η_p	Pump isentropic efficiency	–
η_e	Expander isentropic efficiency	–
$\eta_{th,ORC}$	ORC thermal efficiency	%

Symbols for RSM model

Symbol	**Definition**	**Unit**
A	Coded RSM factor representing pressure	–
B	Coded RSM factor representing temperature	–
C	Coded RSM factor representing current density	–
Y	Polarization-voltage response	V
$\hat{E}$	RSM-predicted polarization voltage	V
$\hat{P}_d$	Power density derived from the RSM-predicted voltage, $\hat{P}_d = i\hat{E}$	W cm^{-2}
β_0	Regression-model intercept	V
$\beta_A, \beta_B, \beta_C$	Linear regression coefficients	V
$\beta_{AB}, \beta_{AC}, \beta_{BC}$	Two-factor interaction coefficients	V
$\beta_{AA}, \beta_{BB}, \beta_{CC}$	Quadratic regression coefficients	V

References

1. Manzo, D.; Thai, R.; Le, H.T.; Venayagamoorthy, G.K. Fuel cell technology review: Types, economy, applications, and vehicle-to-grid scheme. *Sustain. Energy Technol. Assess.* **2025**, *75*, 104229. [CrossRef]
2. Abedin, T.; Pasupuleti, J.; Paw, J.K.S.; Tak, Y.C.; Mahmud, M.; Abdullah, M.P.; Nur-E-Alam, M. Proton exchange membrane fuel cells in electric vehicles: Innovations, challenges, and pathways to sustainability. *J. Power Sources* **2025**, *640*, 236769. [CrossRef]
3. Ying, J.; Liu, T.; Wang, Y.; Guo, M.; Shen, Q.; Lin, Y.; Yu, J.; Yu, Z. Perspectives on membrane development for high temperature proton exchange membrane fuel cells. *Energy Fuels* **2024**, *38*, 6613–6643. [CrossRef]
4. Wu, Q.; Dong, Z.; Zhang, X.; Zhang, C.; Iqbal, A.; Chen, J. Towards more efficient PEM fuel cells through advanced thermal management: From mechanisms to applications. *Sustainability* **2025**, *17*, 943. [CrossRef]
5. Hua, Z.; Wu, J.; Tang, J.; Cao, X.; Xu, J.; Cai, S.; Tu, Z. Advanced multi-recovery techniques for enhancing efficiency in hydrogen fuel cell-based energy systems: An empirical study. *Energy Convers. Manag.* **2025**, *341*, 120004. [CrossRef]
6. Zhou, Z.; Zholobko, O.; Wu, X.-F.; Aulich, T.; Thakare, J.; Hurley, J. Polybenzimidazole-based polymer electrolyte membranes for high-temperature fuel cells: Current status and prospects. *Energies* **2021**, *14*, 135. [CrossRef]
7. Wang, A.; Wu, J.; Li, J.; He, W.; Li, W.; Li, J.; Zhang, L.; Zhang, T.; Zhang, H. High conductivity pyridine-containing polybenzimidazole high-temperature proton exchange membranes for fuel cells. *Energy Technol.* **2026**, *14*, e70502. [CrossRef]
8. El Idi, M.M.; Ankouni, M.; Ben Haj Slama, R.; Affonso Nobrega, P.; Hajjar, A.; Atli, A. Critical review of the latest advances in thermal management techniques for PEM fuel cells. *Renew. Sustain. Energy Rev.* **2026**, *226*, 116199. [CrossRef]
9. Seselj, N.; Cleemann, L.N.; Torres, T.; Azizi, K. Advancing HT-PEM fuel cell technology: Durability and performance under start–stop conditions. *J. Mater. Chem. A* **2025**, *13*, 40500–40536. [CrossRef]
10. Wilberforce, T.; Olabi, A.G.; Muhammad, I.; Alaswad, A.; Sayed, E.T.; Abo-Khalil, A.G.; Maghrabie, H.M.; Elsaid, K.; Abdelkareem, M.A. Recovery of waste heat from proton exchange membrane fuel cells—A review. *Int. J. Hydrogen Energy* **2024**, *52*, 933–972. [CrossRef]
11. Veza, I. Fuel-cell thermal management strategies for enhanced performance: Review of fuel-cell thermal management in proton-exchange membrane fuel cells (PEMFCs) and solid-oxide fuel cells (SOFCs). *Hydrogen* **2025**, *6*, 65. [CrossRef]

12. Matuszewska, D. Solar Organic Rankine Cycle (ORC) systems: A review of technologies, parameters, and applications. *Energies* **2024**, *17*, 5106. [CrossRef]
13. Sánchez, F.D.; Barba Salvador, J.; Mata Montes, C. Organic Rankine Cycle system review: Thermodynamic configurations, working fluids, and future challenges in low-temperature power generation. *Energies* **2025**, *18*, 6561. [CrossRef]
14. Gonidaki, D.; Bellos, E. A detailed review of Organic Rankine Cycles driven by combined heat sources. *Energies* **2025**, *18*, 526. [CrossRef]
15. Kumi, E.N.; Enweremadu, C.C. Thermodynamic exploration of hybrid renewable ORC systems using HFO-based nanofluid zeotropic mixtures. *J. Therm. Anal. Calorim.* **2026**, *151*, 2651–2668. [CrossRef]
16. Hu, X.; Ma, T.; Dong, S.; Zhang, C.; Zhuang, W.; Zhang, T. Design and selection of working fluids for ORC system using computer-aided molecular design and group contribution method. *Appl. Therm. Eng.* **2025**, *274*, 126593. [CrossRef]
17. Kaushik, A.S.; Bhogilla, S.S.; Muthukumar, P. Thermal integration of proton exchange membrane fuel cell with recuperative Organic Rankine Cycle. *Int. J. Hydrogen Energy* **2021**, *46*, 14748–14756. [CrossRef]
18. Wang, C.; Li, Q.; Wang, C.; Zhang, Y.; Zhuge, W. Thermodynamic analysis of a hydrogen fuel cell waste heat recovery system based on a zeotropic Organic Rankine Cycle. *Energy* **2021**, *232*, 121038. [CrossRef]
19. Lu, X.; Du, B.; Zhu, W.; Yang, Y.; Xie, C.; Tu, Z.; Zhao, B.; Zhang, L.; Song, J.; Deng, Z. Thermodynamic and dynamic analysis of a hybrid PEMFC-ORC combined heat and power (CHP) system. *Energy Convers. Manag.* **2023**, *292*, 117408. [CrossRef]
20. Zhou, D.; Nie, H.; Hou, X. Performance evaluation and optimization of proton exchange membrane fuel cell-organic Rankine cycle (PEMFC-ORC) system. *Appl. Therm. Eng.* **2026**, *286*, 129377. [CrossRef]
21. Taweekayujan, S.; Prasertcharoensuk, P.; Chen, Y.-S.; Arpornwichanop, A. Enhancing methanol-to-power: A comprehensive evaluation of an integrated methanol-reforming, high-temperature proton exchange membrane fuel cell, and organic Rankine cycle system. *Energy* **2025**, *321*, 135301. [CrossRef]
22. Xu, S.; Leng, S.; Xie, J.; Liu, Z.; Li, C.; Wang, J.; Chen, Z.; Liao, M.; Qin, J. Performance evaluation and optimization of a distributed generation system integrating high-temperature proton exchange membrane fuel cell and recuperative-regenerative Organic Rankine Cycle. *Energy* **2025**, *319*, 134967. [CrossRef]
23. Gu, Z.; Shi, Y.; Wu, P. Experimental study on the Organic Rankine Cycle for the recovery of the periodic waste heat source. *Energies* **2025**, *18*, 1458. [CrossRef]
24. Chowdhury, P.R.; Gladen, A.C. Comparative and sensitivity analysis of operating conditions on the performance of a high temperature PEM fuel cell. *Int. J. Hydrogen Energy* **2024**, *50*, 1239–1256. [CrossRef]
25. Zhou, M.; Feistner, J.C.; Li, N.; Araya, S.S.; Cinti, G.; Liso, V. Experimental and numerical investigations of high-temperature PEM fuel cells under different anode dilution levels and varying temperatures. *Int. J. Hydrogen Energy* **2024**, *55*, 1383–1392. [CrossRef]
26. Barbir, F. *PEM Fuel Cells: Theory and Practice*; Elsevier: Amsterdam, The Netherlands, 2005.
27. Jayakody, J.R.P.; Chung, S.H.; Durantino, L.; Zhang, H.; Xiao, L.; Benicewicz, B.C.; Greenbaum, S.G. NMR studies of mass transport in high-acid-content fuel cell membranes based on phosphoric acid and polybenzimidazole. *J. Electrochem. Soc.* **2007**, *154*, B242–B246. [CrossRef]
28. Franke, F.; Link, A.; Kazula, S. Evaluation of heat transfer technologies for high temperature polymer electrolyte membrane fuel cells as primary power source in a regional aircraft. *CEAS Aeronaut. J.* **2026**, *17*, 1037–1061. [CrossRef]
29. Javed, S.; Tiwari, A.K. Performance analysis of zeotropic mixture as a working fluid for medium temperature in regenerative Organic Rankine Cycle. *Process Saf. Environ. Prot.* **2023**, *179*, 864–872. [CrossRef]
30. Lu, P.; Chen, K.; Luo, X.; Wu, W.; Liang, Y.; Chen, J.; Chen, Y. Experimental and simulation study on a zeotropic ORC system using R1234ze(E)/R245fa as working fluid. *Energy* **2024**, *292*, 130453. [CrossRef]
31. Lemmon, E.W.; Huber, M.L.; McLinden, M.O. *NIST Standard Reference Database 23: Reference Fluid Thermodynamic and Transport Properties—REFPROP, Version 8.0*; National Institute of Standards and Technology, Standard Reference Data Program: Gaithersburg, MD, USA, 2007.
32. Box, G.E.P.; Behnken, D.W. Some New Three Level Designs for the Study of Quantitative Variables. *Technometrics* **1960**, *2*, 455–475. [CrossRef]
33. Zhang, J.; Tang, Y.; Song, C.; Zhang, J. Polybenzimidazole-membrane-based PEM fuel cell in the temperature range of 120–200 °C. *J. Power Sources* **2007**, *172*, 163–171. [CrossRef]

Disclaimer/Publisher's Note: The statements, opinions and data contained in all publications are solely those of the individual author(s) and contributor(s) and not of MDPI and/or the editor(s). MDPI and/or the editor(s) disclaim responsibility for any injury to people or property resulting from any ideas, methods, instructions or products referred to in the content.